Non-linear time domain analysis of cross-flow vortex-induced vibrations

M.J. Thorsen[a,*], S. Sævik[a], C.M. Larsen[a]

[a]*Department of Marine Technology, Norwegian University of Science and Technology, 7491 Trondheim, Norway*

Abstract

A previously proposed hydrodynamic load model for time domain simulation of cross-flow vortex-induced vibrations (VIV) is modified and combined with Morison's equation. The resulting model includes added mass, drag and a cross-flow vortex shedding force which is able to synchronize with the cylinder motion within a specified range of non-dimensional frequencies. It is demonstrated that the hydrodynamic load model provides a realistic representation of the cross-flow energy transfer and added mass for different values of the non-dimensional frequency and amplitude. Furthermore, it gives a reasonable approximation of the experimentally observed drag amplification. The load model is combined with a non-linear finite element model to predict the cross-flow VIV of a steel catenary riser in two different conditions: VIV due to a stationary uniform flow and VIV caused by periodic oscillation of the riser top end. In the latter case, the prescribed motion leads to an oscillating relative flow around the riser, causing an irregular response. The simulation results are compared to experimental measurements, and it is found that the model provides highly realistic results in terms of r.m.s. values of strains and frequency content, although some discrepancies are seen.

Keywords: Vortex-induced vibrations, Dynamic time domain analysis, Nonlinear finite element model

1. Introduction

Elastic cylinders in fluid flow experience structural oscillations caused by vortex shedding, known as vortex-induced vibrations (VIV) [1]. The classic example is the elastically mounted rigid cylinder in a steady incoming flow, free to oscillate in the cross-flow direction [2]. In the offshore industry however, one is typically concerned with VIV of long slender structures such as risers and free spanning pipelines. Here, the VIV response may consist of several higher modes, in-line and cross-flow oscillations, and a combination of traveling and standing waves [3]. In addition, the incoming undisturbed flow may vary along the cylinder span.

To accurately predict riser VIV, two things must be in place. The first is a mathematical model that, given the hydrodynamic forces acting on the structure, can accurately predict the structural response. Secondly, one must be able to calculate the hydrodynamic forces along the structure, which will depend on the motion of the riser. The first part of the problem can be handled using the finite element method (FEM). If non-linear FEM is utilized, potentially important effects such as large displacements, time-varying geometric stiffness and changing boundary conditions may also be dealt with. The second part of the problem can be solved using computational fluid dynamics [4], but the necessary computer resources are large. Therefore, alternative semi-empirical methods have been developed, such as VIVANA, VIVA and SHEAR7 [5, 6, 7]. These are based on hydrodynamic coefficients measured in experiments, which is combined with a structural model to predict the VIV response in the frequency domain. Because the analysis is performed in the frequency domain, these methods require a linear structural model and stationary conditions (i.e. constant current velocity in time).

*Corresponding author. Tel.: +47 735 50881
Email address: mats.j.thorsen@ntnu.no (M.J. Thorsen)

The limitations of the frequency domain methods prohibit realistic modeling of some problems. As an example, consider a steel catenary riser (SCR) suspended from a floating platform. The top end will be subjected to wave induced motions, which will cause the riser tension, and hence the geometric stiffness, to vary with time. Close to the bottom, a segment of the riser will go in and out of contact with the seabed, causing time-varying boundary conditions. If the wave induced motions are sufficiently large, vortex shedding will initiate due to the relative oscillatory flow [8]. Hence, the VIV response can be stationary in some parts (due to current) while in other parts it may be intermittent (due to relative oscillatory flow). In addition, internal slug flow may also cause riser vibrations [9], which will interact with the VIV response. To capture all these effects, a non-linear time domain analysis is required.

Several models exist which can be used to simulate VIV in time domain. One such model is the wake-oscillator, which is based on the assumption that the lift coefficient can be described by a forced Van der Pol oscillator. This idea was first suggested by Bishop and Hassan [10], and has been modified by many others since then (see e.g. [11] for a review). Such models have been used in a large number of studies, for instance to investigate the behavior of flexible structures with geometric nonlinearities [12]. However, it is difficult to find a consistent set of wake-oscillator parameters suitable for both forced and free vibrations. [13]. Other time domain models have been developed by Lie [14], Finn et al. [15], Mainçon [16] and Xue et al. [17].

An alternative semi-empirical model for time domain simulation of VIV has been under development by Thorsen et al. [18, 19, 20, 21, 22], and the present paper is a continuation of this work. In combination with a finite element model, it has been shown that the model can be used to predict VIV of elastic cylinders in various current conditions, including oscillating flow. In these previous studies, the structural model was linear, and the mean in-line drag force was not included. The purpose of the present paper is to introduce a non-linear finite element model (including non-linear soil contact) for the structure, and to include the mean in-line drag forces (and the associated displacements). This should enable highly realistic prediction of the dynamic response of risers and other slender structures due to ocean currents in combination with prescribed oscillatory motions and possibly other loads (ocean waves are not considered here). To illustrate the applicability of the proposed model, it is utilized to simulate the cross-flow VIV of an SCR in two different conditions. The first is VIV due to a stationary incoming uniform flow. Secondly, VIV caused by periodic oscillation of the riser top end is considered. The results are compared to experiments.

2. Hydrodynamic load modeling

2.1. Morison's equation

This paper considers the dynamic response of slender circular structures exposed to currents. In addition, the structure can have velocities and accelerations induced by other loads or prescribed motions. A strip theory approach is used, such that the hydrodynamic force on a cylinder cross-section is calculated from velocities and accelerations at the same cross-section only. The relevant velocity vectors and coordinate system for computing the hydrodynamic force on a cylinder segment is shown in figure 1. The relative flow velocity is $\mathbf{v} = \mathbf{u} - \dot{\mathbf{x}}$, where $\mathbf{u}$ is the incoming flow velocity and $\dot{\mathbf{x}}$ is the velocity of the cylinder cross-section. The relative flow is not necessarily perpendicular to the cylinder, and $\mathbf{v}$ is therefore decomposed into a tangential component $\mathbf{v}_t$ and a normal component $\mathbf{v}_n$. Similarly, the normal component of the flow and structure acceleration is denoted $\dot{\mathbf{u}}_n$ and $\ddot{\mathbf{x}}_n$ respectively. The hydrodynamic drag and inertia forces (per unit length) on a cylinder cross-section is described using the generalized Morison's equation:

$$\mathbf{F}_n = C_M \rho \frac{\pi D^2}{4} \dot{\mathbf{u}}_n - (C_M - 1)\rho \frac{\pi D^2}{4} \ddot{\mathbf{x}}_n + \frac{1}{2} \rho D C_D |\mathbf{v}_n| \mathbf{v}_n. \tag{1}$$

Here, ρ is the water density and D is the cylinder diameter. C_M and C_D are the inertia and drag coefficients in the normal direction, which depend on a number of parameters (see e.g. [23]). Note that equation (1) only gives forces normal to the cylinder, and any tangential forces are neglected.

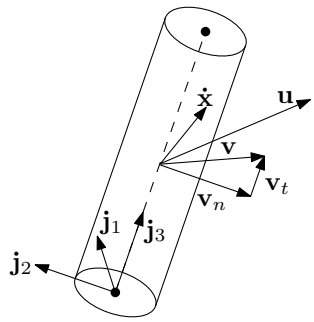

Figure 1: A cylinder segment with local coordinate system and velocity vectors.

2.2. Vortex shedding

A cylinder in a current will be excited by vortex shedding, even if the incoming flow is steady [24]. The flow separates from the cylinder surface and rolls up into vortices on either side, which for Reynolds numbers larger than 40 are unstable, causing alternating vortex shedding and the formation of a vortex street. For a stationary cylinder in a steady flow with velocity U, the vortex shedding frequency is given as $f_s = \mathrm{St}U/D$, where St is the Strouhal number. This depends on the Reynolds number and the cylinder surface roughness, but in the subcritical Reynolds number range, St is fairly constant and close to 0.2. [25]. The fluctuating pressure field associated with the vortex shedding causes oscillating forces both in the direction of the flow (drag) and perpendicular to the flow (lift). In the case of an elastic cylinder, the vortex shedding forces will cause structural vibrations, which in turn alters the surrounding flow and the hydrodynamic forces. An important interaction effect is that the vortex shedding frequency may deviate from the Strouhal frequency (i.e. the frequency for a stationary cylinder), and lock on to the frequency of motion. The synchronization between the cylinder motion and vortex shedding has been experimentally observed and discussed by several researchers, for instance Williamson and Roshko [26].

To represent the vortex shedding forces, a simple empirical model is applied. The present model is based on the work by Thorsen et al. [18, 19, 20, 21, 22], with some modifications. The main reason for modifying the model is that the drag term in Morison's equation will cause damping of vibrations. To illustrate this, consider as an example a cylinder in an incoming steady flow, U. Let the y-axis point in the direction perpendicular to the flow and assume the cylinder is oscillating in the cross-flow direction with a velocity $\dot{y}$, as shown in figure 2. Taking only the drag term from equation (1) into account, the cross-flow component of the drag force is:

$$\begin{aligned} F_y &= -\frac{1}{2}\rho D C_D |\mathbf{v}_n|^2 \sin\theta = -\frac{1}{2}\rho D C_D |\mathbf{v}_n| \dot{y} \\ &= -\frac{1}{2}\rho D C_D \sqrt{U^2 + \dot{y}^2}\,\dot{y}. \end{aligned} \tag{2}$$

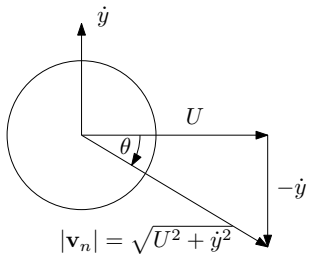

Figure 2: A cylinder in an incoming flow, moving in the cross-flow direction with velocity $\dot{y}$.

It is seen from equation (2) that the cross-flow component of the drag force is always in the direction opposite of the cross-flow cylinder velocity, and will therefore cause damping of vibrations. The previous investigations by Thorsen et al. [18, 19, 20, 21, 22] did not include drag forces, and hydrodynamic damping was introduced by a separate damping model. This damping model is not applicable in the present work, because damping is already included through the drag term in Morison's equation. The question is then if the drag term in Morison's equation is able to represent damping of vortex-induced vibrations? For the sake of simplicity, it will be assumed in the following that this is true. Although it is easy to criticize this assumption, one should remember that it is the net flow of energy between the fluid and structure which is important. This is determined by the power-in from vortex excitation minus the power-out from damping (drag in this case). Therefore, the properties of the damping model is not necessarily important, it is only required that the sum of excitation and damping is correct.

Based on [18], the vortex shedding force on a cylinder strip is expressed as:

$$\mathbf{F}_{\text{exc}} = \frac{1}{2}\rho D C_v |\mathbf{v}_n| (\mathbf{j}_3 \times \mathbf{v}_n) \cos\phi_{\text{exc}}. \tag{3}$$

The force given by equation (3) is perpendicular to $\mathbf{v}_n$ and $\mathbf{j}_3$ (see figure 1), which means that $\mathbf{F}_{\text{exc}}$ points in the direction normal to the relative flow velocity. The magnitude of the force is determined by a dimensionless coefficient, C_v, and the oscillatory behavior is taken into account through the time varying instantaneous phase ϕ_{exc}. Note that a fluctuating drag force (i.e. an excitation force parallel to $\mathbf{v}_n$) is generally also present. This force will cause in-line vibrations of the cylinder, but these are significantly smaller than the cross-flow vibrations [27]. In the present research, focus will be on cross-flow vibrations, and the fluctuating drag is neglected.

As the vortex shedding force oscillates, the phase ϕ_{exc} changes continuously, and goes from 0 to 2π in one complete cycle. If the frequency of the force was some constant f_{exc}, the rate of change of the phase angle would be $\dot{\phi}_{\text{exc}} = 2\pi f_{\text{exc}}$. This is however not the case, as the frequency is influenced by, and will in some cases synchronize with the cylinder motion. A synchronization model was presented by Thorsen et al. [18], where the instantaneous frequency of the excitation force was expressed as a function of the phase difference between the cylinder cross-flow velocity and the force itself. This type of model is also adopted here, but for simplicity and flexibility, the non-dimensional frequency curve is now described analytically as:

$$\hat{f}_{exc} = \hat{f}_0 + \Delta\hat{f}\sin(\phi_{\dot{y}_{\text{rel}}} - \phi_{\text{exc}}) = \hat{f}_0 + \Delta\hat{f}\sin\theta. \tag{4}$$

This type of synchronization model is known as the Kuramoto model, which was originally used to study collective synchronization in large systems of oscillators [28]. In the present context, $\phi_{\dot{y}_{\text{rel}}}$ is the instantaneous phase of the relative cross-flow velocity of the cylinder (to be defined in section 2.2.1), and $\theta = \phi_{\dot{y}_{\text{rel}}} - \phi_{\text{exc}}$ is the phase difference between the relative cross-flow cylinder velocity and the vortex excitation force. $\hat{f}_0$ corresponds to the non-dimensional frequency at the center of the synchronization range, while $\Delta\hat{f}$ describes how much the vortex shedding frequency is allowed to deviate from $\hat{f}_0$. This means that the vortex shedding will synchronize with the cylinder motion for non-dimensional frequencies between $\hat{f}_0 - \Delta\hat{f}$ and $\hat{f}_0 + \Delta\hat{f}$. The present synchronization model is compared to the previously used curve [22] in figure 3. The parameters in the model is taken as $\hat{f}_0 = 0.18$ and $\Delta\hat{f} = 0.08$, as these values give approximately the same synchronization range as the previously used curve, i.e. from $\hat{f} = 0.10$ to $\hat{f} = 0.26$. The previously used curve was obtained from excitation coefficient data and has been validated through comparison with several experiments [18, 19, 20, 21, 22]. However, the new model introduced here gives more flexibility, as the parameters $\hat{f}_0$ and $\Delta\hat{f}$ can be easily changed. Although constant values are used in this paper, it is expected that these may vary with the Reynolds number and cylinder roughness, and this flexibility is therefore desired. The new new synchronization model is expected to provide similar results as the previously used curve, because it captures the main features, such as maximum frequency when $\theta = \pi/2$ and minimum frequency when $\theta = -\pi/2$.

When the non-dimensional excitation frequency is found, the rate of change of ϕ_{exc} is computed as:

$$\dot{\phi}_{\text{exc}} = 2\pi f_{\text{exc}} = \frac{2\pi|\mathbf{v}_n|}{D}\hat{f}_{\text{exc}}. \tag{5}$$

The idea behind the synchronization model is that the phase difference $\phi_{\dot{y}_{\mathrm{rel}}} - \phi_{\mathrm{exc}}$ gives information about who is "leading" the oscillation. For example, if the phase difference is positive, the cylinder velocity is ahead, which means the excitation force must increase its frequency to catch up.

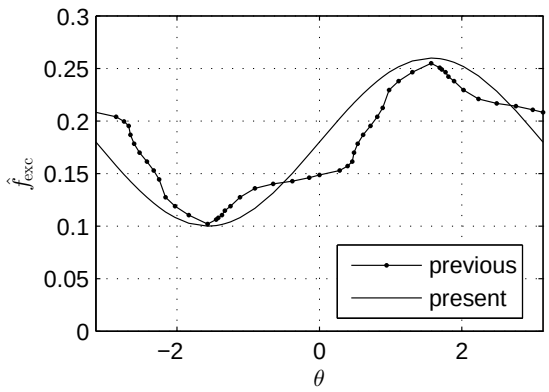

Figure 3: Non-dimensional frequency of the excitation force as a function of the phase difference between the relative cross-flow cylinder velocity and the vortex excitation force. The present analytical model is shown together with the previously used curve [22].

2.2.1. Computing the phase of the relative cross-flow cylinder velocity

The instantaneous phase of the relative cross-flow velocity of the cylinder strip appears in equation (4), and must be computed for every time step of the simulation (and for every cylinder strip/element in the model). The relative cross-flow cylinder velocity is defined as:

$$\dot{y}_{\mathrm{rel}} = \dot{\mathbf{x}} \cdot \mathbf{n}, \tag{6}$$

where $\mathbf{n}$ is a unit vector normal to $\mathbf{v}_n$, which is found as

$$\mathbf{n} = \frac{\mathbf{j}_3 \times \mathbf{v}_n}{|\mathbf{v}_n|}. \tag{7}$$

Similarly, the relative cross-flow cylinder acceleration is found as

$$\ddot{y}_{\mathrm{rel}} = \ddot{\mathbf{x}} \cdot \mathbf{n}. \tag{8}$$

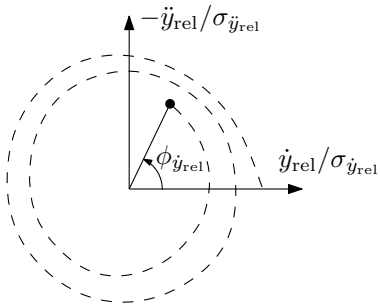

Figure 4: The phase diagram illustrates how the instantaneous phase of the relative cross-flow velocity is found.

The phase of $\dot{y}_{\mathrm{rel}}$ is calculated using the phase portrait concept [18]. This can be visualized by plotting the normalized relative cross-flow velocity on a horizontal axis and the normalized relative cross-flow acceleration with a negative sign on a vertical axis, as shown in figure 4. The velocities/accelerations are normalized by

their respective root mean square (r.m.s.) values. For generality, the r.m.s. is allowed to vary with time and is hence calculated over a finite interval backwards in time. Let n_m be the number of time steps in the interval, such that $T_m = (n_m - 1)\Delta t$ is the length of the interval. Then, the r.m.s. of $\dot{y}_{\mathrm{rel}}$ at time t_i may be found from the following expression:

$$\sigma_{\dot{y}_{\mathrm{rel}}}(t_i) = \sqrt{\frac{1}{n_m} \sum_{j=i-n_m+1}^{i} (\dot{y}_{\mathrm{rel}}(t_j))^2}, \tag{9}$$

Because computing the sum in equation (9) every time step would be time consuming, a more efficient approximate method is used. By splitting the sum in two parts, the r.m.s. can be written as:

$$\sigma_{\dot{y}_{\mathrm{rel}}}(t_i) = \sqrt{\frac{1}{n_m} \sum_{j=i-n_m+1}^{i-1} (\dot{y}_{\mathrm{rel}}(t_j))^2 + \frac{1}{n_m}(\dot{y}_{\mathrm{rel}}(t_i))^2}. \tag{10}$$

By introducing the approximation

$$\sum_{j=i-n_m+1}^{i-1} (\dot{y}_{\mathrm{rel}}(t_j))^2 \approx (n_m - 1)(\sigma_{\dot{y}_{\mathrm{rel}}}(t_{i-1}))^2, \tag{11}$$

the new r.m.s. value can be calculated from the previous, in combination with the new relative velocity:

$$\sigma_{\dot{y}_{\mathrm{rel}}}(t_i) \approx \sqrt{\frac{n_m - 1}{n_m}(\sigma_{\dot{y}_{\mathrm{rel}}}(t_{i-1}))^2 + \frac{1}{n_m}(\dot{y}_{\mathrm{rel}}(t_i))^2}. \tag{12}$$

To verify that the approximate expression (12) provides satisfactory accuracy, a test is performed where the time varying r.m.s. of a given time series are compared to the exact result (i.e. calculated by performing the sum over all the data points in the time interval). The results are shown in figure 5. The time series is taken from a simulation with the present model. It is seen that the curves calculated using the approximate expression follow the exact results closely, and it is concluded that the approximate expression provides sufficient accuracy for the present application, which is to normalize the phase diagram (see figure 4).

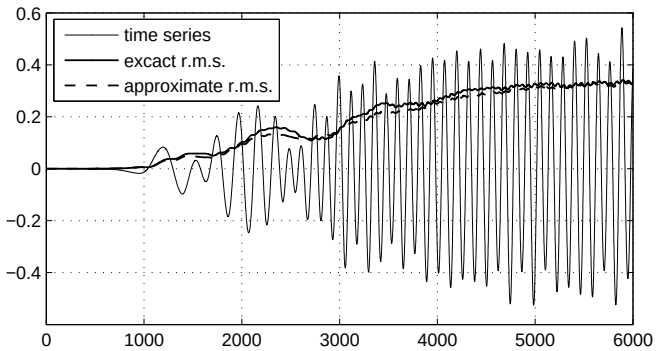

Figure 5: Comparison between the exact and approximate expression for the moving r.m.s. of a time series. In this example, $n_m = 500$.

2.3. Total hydrodynamic force

To summarize the above, the total hydrodynamic force per unit length on a cylinder section is given as the sum of equation (1) and (3):

$$\mathbf{F} = C_M \rho \frac{\pi D^2}{4} \dot{\mathbf{u}}_n - (C_M - 1)\rho \frac{\pi D^2}{4} \ddot{\mathbf{x}}_n + \frac{1}{2}\rho D C_D |\mathbf{v}_n| \mathbf{v}_n + \frac{1}{2}\rho D C_v |\mathbf{v}_n| (\mathbf{j}_3 \times \mathbf{v}_n) \cos\phi_{\mathrm{exc}}. \tag{13}$$

The above equation is referred to as "the hydrodynamic force model". The first term is the force due to water particle acceleration, the second term is the added mass force resulting from cylinder acceleration, the third term is drag and the last is due to vortex shedding.

3. Testing the hydrodynamic force model

3.1. Introduction

As the proposed hydrodynamic force model is semi-empirical, it is important to test its predictive capabilities. To accurately predict VIV, it is necessary to have a good description of the energy transfer (between the fluid and the oscillating cylinder) and the added mass variations. The mean drag force is also of interest due to its role in determining the static deflection and tension in a slender structure such as a riser. It should be kept in mind that the goal of this research has been to develop a model which is as simple as possible, but still able to include the most important effects. A simple model is easier to use in practical engineering calculations, and is also easier to understand. Although it is certainly desirable to include every physical effect, it is recognized that reaching such a goal would probably require a very complex model. Because of this, it is assumed here that the hydrodynamic coefficients C_M, C_D and C_v (ref. equation (13)) can be considered constant when the Reynolds number is constant. In other words, the coefficients do not depend on e.g. the VIV frequency or amplitude. This is in contrast to the previous work by Thorsen et al. [18, 19, 20, 21, 22], where C_v was a function of y_0/D (but not frequency). However, the Reynolds number dependency must be accounted for, which is discussed in section 5. In the following, some basic examples are used to demonstrate that the model provides reasonable results compared to experimental observations, and also how the choice of C_v influences the results.

3.2. Energy transfer

The energy transfer between the fluid and structure during VIV is important to the response amplitude. A useful dimensionless measure of the cross-flow energy transfer is the lift coefficient in phase with the cylinder velocity, defined as:

$$C_{y,v} = \lim_{T\to\infty} \frac{2}{T} \int_0^T C_y(t) \cos(\omega t) dt, \tag{14}$$

where $C_y(t) = F_y/(0.5\rho D U^2)$ is the (total) lift coefficient. Here it has been assumed that the cross-flow displacement of the cylinder is $y = y_0 \sin(\omega t)$. If there is no in-line motion and the incoming flow velocity is U, the cross-flow hydrodynamic force is according to the present model:

$$F_y = \frac{1}{2}\rho D C_v \sqrt{U^2 + \dot{y}^2} U \cos\phi_{\text{exc}} - \frac{1}{2}\rho D C_D \sqrt{U^2 + \dot{y}^2}\dot{y} - (C_M - 1)\rho \frac{\pi D^2}{4}\ddot{y}. \tag{15}$$

To investigate the performance of the model, simulations have been performed, where a rigid cylinder is oscillated in the cross-flow direction with different y_0/D and $\hat{f} = fD/U = \omega D/(2\pi U)$. The resulting lift coefficient in phase with cylinder velocity is shown in figure 6. For these simulations, $C_D = C_v = 1.2$ and $C_M = 2$. Note however that the inertia force is always out of phase with $\dot{y}$, and does not contribute to $C_{y,v}$. It is seen that for small amplitudes, $C_{y,v}$ is positive between approximately $\hat{f} = 0.1$ and $\hat{f} = 0.26$. In the present model, the range of positive excitation is determined by the parameters $\hat{f}_0$ and $\Delta\hat{f}$ (ref. equation (4)). When the amplitude increases, so does the energy loss due to drag, and $C_{y,v}$ drops. The excitation zone extends up to a maximum of $y_0/D \approx 0.8$. Above this level, $C_{y,v}$ is negative, which means that vibrations will be damped. To demonstrate how the choice of C_v affects the results, the above simulations are repeated with $C_v = 1.0$ and $C_v = 1.4$. The zero excitation curve (i.e. $C_{y,v} = 0$) for the different realizations are shown and compared to the experimental results by Gopalkrishnan [29] in figure 7. Clearly, an increase in C_v causes the positive excitation region to extend upwards to higher amplitude. However, the frequency range for synchronization remains unchanged. It is seen that the present model predicts a single connected excitation region, while Gopalkrishnan found two separate regions. Merging the two regions into one can

be considered an approximation, but previous research have shown that a single excitation region may in fact be more accurate for flexible beams [30]. It is also noted that the upper and lower boundaries of the excitation region, in terms of dimensionless frequency, do not match perfectly with Gopalkrishnan's results. A better agreement could have been obtained by changing the parameters $\hat{f}_0$ and $\Delta\hat{f}$ in the synchronization model. However, there are uncertainties related to the width of the excitation region (other experiments typically show slightly different results), and therefore it seems unnecessary to strive for perfect agreement with a single experiment.

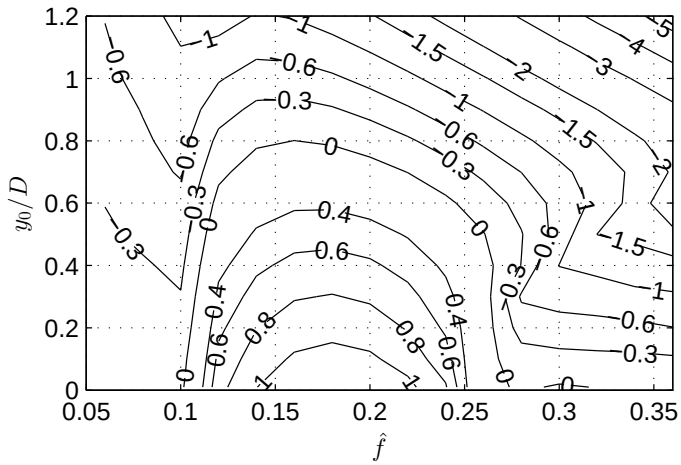

Figure 6: Lift coefficient in phase with cylinder velocity predicted by the model, using $C_D = C_v = 1.2$.

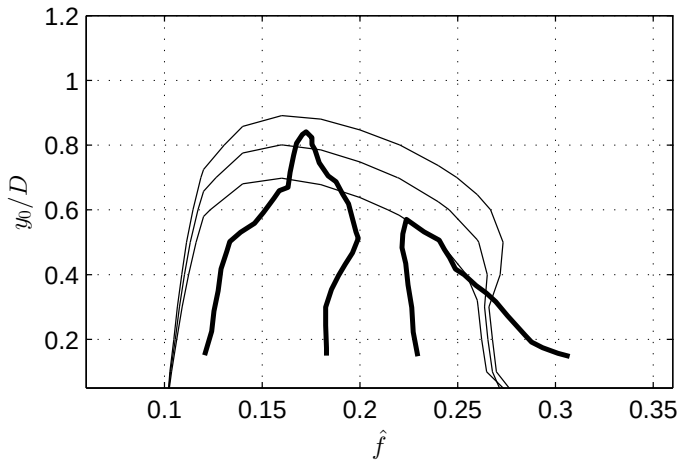

Figure 7: The curve corresponding to zero energy transfer, i.e. $C_{y,v} = 0$, calculated using $C_v = 1.0$ (the smallest region), $C_v = 1.2$ (the intermediate region) and $C_v = 1.4$ (the largest region). The thick curve is from experiments by Gopalkrishnan [29].

3.3. Added mass

The added mass is a measure of the hydrodynamic force component in phase with the acceleration of the cylinder. The added mass is especially important in VIV, as experiments have shown that the VIV response occurs at a true natural frequency when the added mass is taken into account [31]. This means that the oscillation frequency can be calculated if the added mass is known, and this fact is utilized in other VIV

prediction tools such as VIVANA [5]. Solving for the unknown vibration frequency is however not straight forward because the added mass depends on both y_0/D and $\hat{f}$. Using the present method, this problem is circumvented because the response is computed directly in the time domain, without any prior knowledge of the vibration frequency. With reference to equation (13), there are two terms contributing to the total added mass: the added mass term from Morison's equation, and the vortex shedding force. The latter may be partially in phase with the cylinder acceleration (the actual phase difference will be determined by the synchronization model, ref. equation (4)), and will influence the total added mass. The added mass is usually expressed as a dimensionless coefficient $C_a = M_a/(0.25\rho\pi D^2)$, where M_a is the total added mass of the cylinder. When the time series of the force and acceleration are known (from experiment or simulation), the added mass coefficient may be found as:

$$C_a = -\frac{8}{\rho\pi D^2\omega^4 y_0^2} \lim_{T\to\infty} \frac{1}{T}\int_0^T F_y(t)\ddot{y}(t)dt. \tag{16}$$

The added mass predicted by the present model was found by simulating a rigid cylinder with a prescribed cross-flow oscillation, using different y_0/D and $\hat{f}$, and the results are shown in figure 8. It is seen that the model predicts positive added mass for non-dimensional frequencies higher than 0.15 approximately, while for lower frequencies, the added mass is negative. This is in agreement with the observations made by Gopalkrishnan [29]. However, the model predicts large negative values of added mass when both the frequency and amplitude is low, and this is not seen in experiments. This discrepancy may be unimportant, because the resulting added mass force is small when the frequency and amplitude is small. To investigate this further, the model is used to simulate the cross-flow VIV of a spring mounted cylinder, which means solving the 1-DOF dynamic equilibrium equation:

$$m\ddot{y} + c\dot{y} + ky = F_y(t), \tag{17}$$

where m is the cylinder (structural) mass per unit length, c is the structural damping and k is the spring stiffness. The mass ratio is set to $m/(0.25\rho\pi D^2) = 1.66$ and the damping ratio (in air) to 0.1 %, which is the same as in the free vibration experiment performed by Vikestad [31]. A number of simulations are run, with increasing reduced velocity, $U_r = U/(f_0 D)$, where f_0 is the natural frequency of the cylinder in still water. For each simulation, the transient is removed before the total added mass coefficient are computed according to equation (16). The results are shown and compared to Vikestad's in figure 9. It is seen that the model predicts the total added mass coefficient with high accuracy for $U_r > 5.5$. Cross-flow VIV is known to initiate around $U_r = 4$, reaching the maximum vibration amplitude when $6 < U_r < 8$ approximately, depending on the mass ratio of the cylinder. Hence, the model predicts the correct added mass over the most important range of reduced velocities, i.e. where the vibrations are expected to be largest. The results are less accurate for $U_r < 5$, but in this region the vibration amplitude is relatively small.

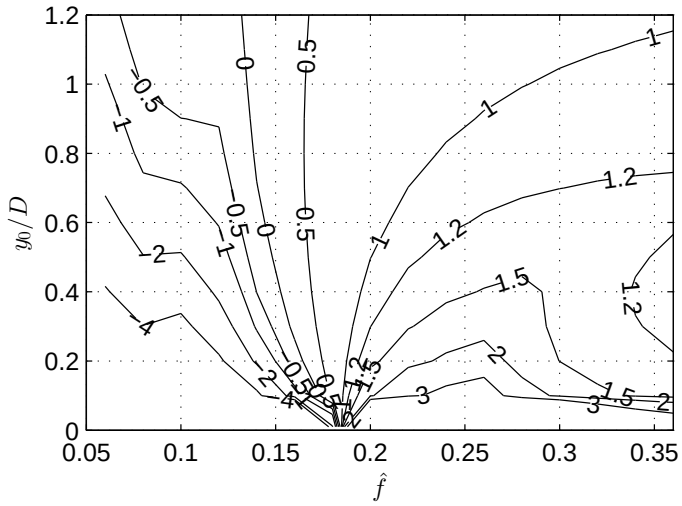

Figure 8: Added mass coefficient predicted by the model, using $C_D = C_v = 1.2$ and $C_M = 2$.

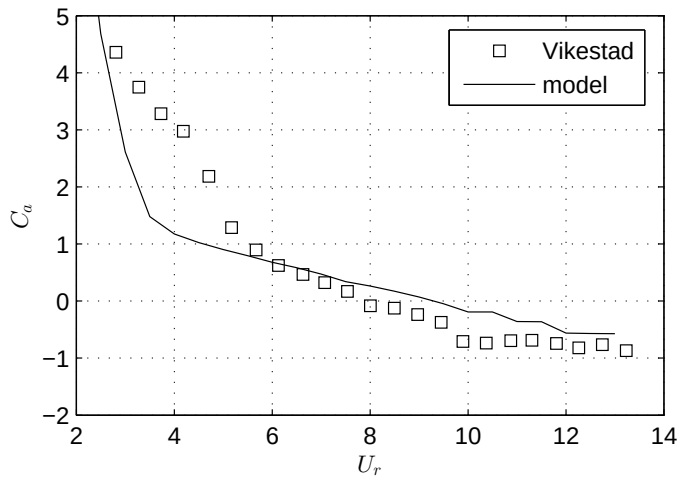

Figure 9: Added mass coefficient for free cross-flow vibration of spring mounted cylinder. The dotted line is predicted by the model, using $C_D = C_v = 1.2$ and $C_M = 2$, while the squares are from the experiments by Vikestad [31].

3.4. Amplitude and phase of lift coefficient

The preceding sections focused on the lift coefficient components in phase with the cylinder velocity and acceleration. However, the lift coefficient may also be expressed in terms of its total magnitude and a phase angle. This approach was used by Carberry et al. [32] , who expressed the total lift force as:

$$F_y = \frac{1}{2}\rho D U^2 C_L \sin(2\pi f t + \phi_{\text{lift}}). \tag{18}$$

The cross-flow displacement was taken as $y = y_0 \sin(2\pi f t)$, such that ϕ_{lift} is the phase angle between the cross-flow displacement of the cylinder and the lift force component at the frequency of oscillation. Carberry et al. presents how the phase angle and total lift coefficient varies with the oscillation frequency at a constant $y_0/D = 0.5$, and compares their result to those of Sarpkaya [33], Gopalkrishnan [29], Mercier [34] and Staubli [35]. The purpose here is to investigate how the present hydrodynamic load model predicts the total lift coefficient and phase angle compared to all these experiments. To do this, simulation of forced cross-flow vibration is performed as previously. The initial transient is removed, and the lift coefficient in phase with the cylinder velocity is calculated according to equation (14). Similarly, the component in phase with the cylinder displacement is found as:

$$C_{y,d} = \lim_{T\to\infty} \frac{2}{T} \int_0^T C_y(t) \sin(\omega t) dt. \tag{19}$$

The total lift coefficient is then found as $C_L = \sqrt{C_{y,v}^2 + C_{y,d}^2}$ and the phase angle is found from $\tan\phi_{\text{lift}} = C_{y,v}/C_{y,d}$. The results are plotted and compared to the mentioned experiments in figure 10 and 11, where the frequency of vibration has been normalized by the Strouhal frequency. From figure 10, it is seen that there is a transition in the phase angle as the oscillation frequency approaches the Strouhal frequency. When the oscillation frequency is low, ϕ_{lift} is approximately 225°, and for high frequencies the phase angle is close to zero. Looking at the experimental results, the change in phase angle happens quite suddenly around $f/f_s = 0.8$, while the model predicts a smoother transition, beginning around $f/f_s = 0.6$. Moving on to figure 11, the magnitude of the lift coefficient is small for the lower frequencies. This is because the vortex shedding force is not synchronized with the cylinder motion. In addition, the cross-flow component of the drag force is small. As the frequency is increased towards f_s, synchronization causes C_L to rise. When the frequency is increased further, the drag and added mass forces increase, causing very high values of C_L. Taking the scatter in the experimental results into account, the present model gives a good approximation of how the phase angle and the total lift coefficient changes as the oscillation frequency is varied around the Strouhal frequency.

3.5. Mean drag

For a cylinder oscillating with a cross-flow motion $y = y_0 \sin\omega t$, the force per unit length in the flow direction may generally be expressed as $F_x = \bar{F}_x + \tilde{F}_x$, where $\bar{F}_x$ is the mean and $\tilde{F}_x$ is the fluctuating drag. The magnitude of the mean drag is usually given as a dimensionless mean drag coefficient, defined as:

$$\bar{C}_D = \frac{\bar{F}_x}{0.5\rho D U^2}. \tag{20}$$

According to the present model, the in-line component of the hydrodynamic force is in this situation (from equation (13)):

$$F_x = \frac{1}{2}\rho D C_D \sqrt{U^2 + \dot{y}^2} U + \frac{1}{2}\rho D C_v \sqrt{U^2 + \dot{y}^2} \dot{y} \cos\phi_{\text{exc}}. \tag{21}$$

The first term in the above equation is the in-line component of the drag force in Morison's equation, and it is seen that this term increases with the cross-flow velocity. The second term is due to the vortex shedding force, which is also seen to increase with the cross-flow velocity. However, the mean value of the second term

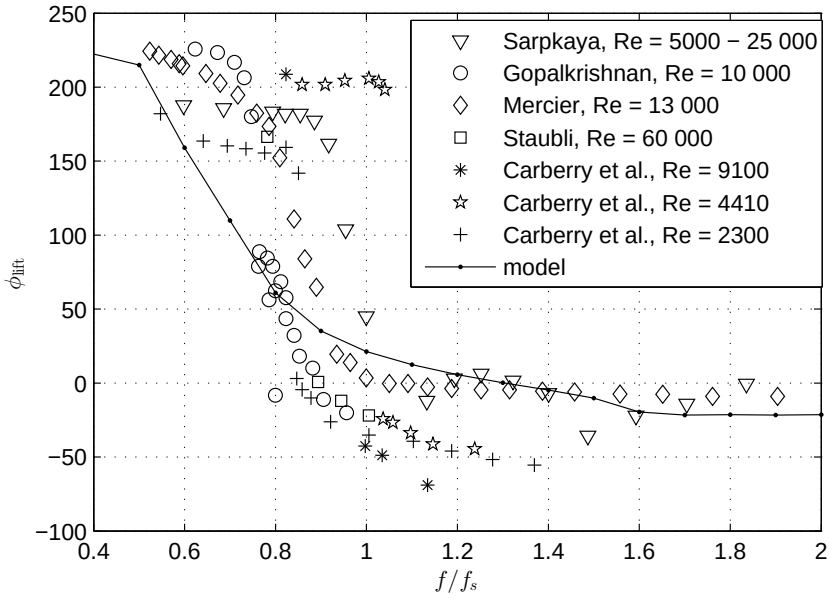

Figure 10: Phase angle between the total lift force and the cross-flow cylinder displacement as a function of frequency at $y_0/D = 0.5$. The solid line is predicted by the model using $C_D = C_v = 1.2$ and $C_M = 2$, while the symbols represent the experiments by Sarpkaya [33], Gopalkrishnan [29], Mercier [34], Staubli [35] and Carberry et al. [32]. The experimental data was taken from [32].

will be zero if $\cos\phi_{\text{exc}}$ is uncorrelated with $\dot{y}$. In other words, the vortex shedding force only contributes to the mean drag if it is synchronized with the cylinder velocity.

The mean drag coefficient predicted by the present model was found by simulating a rigid cylinder with a prescribed cross-flow oscillation, using different y_0/D and $\hat{f}$, and the results are shown in figure 12. In this example, $C_D = C_v = 1.2$. This value of C_D agrees with that of a stationary cylinder at Re $\approx$ 10 000. With reference to figure 12, it is seen that the mean drag is essentially equal to 1.2 for small amplitudes and/or frequencies. This is because the cylinder velocity is small compared to the incoming flow, which means that $\bar{C}_D \to C_D$, according to equation (21). When y_0/D or $\hat{f}$ is increased, so does the mean drag, and for cases where both y_0/D and $\hat{f}$ are large, $\bar{C}_D$ can reach very high values. This behavior is also seen in experiments, and figure 13 shows a comparison between the simulated results and experimental observations by Gopalkrishnan [29] for $y_0/D = 0.75$. The comparison illustrates that the model only gives an approximation of how the mean drag varies, and the discrepancies indicate that better agreement could have been found by changing the model parameters.

3.6. Summary

Some of the most important points illustrated above is summarized as follows:

i) The energy transferred to the vibrating cylinder (quantified through the lift coefficient in phase with the cylinder velocity) depends on C_D and C_v. The drag coefficient determines the damping, which increases together with the vibration amplitude and frequency. With reference to figure 6, the drag force has an impact on $C_{y,v}$ for all values of y_0/D and $\hat{f}$. The vortex shedding force on the other hand, only affects $C_{y,v}$ in the region where the vortex shedding is synchronized with the cylinder motion. Increasing C_v extends the positive excitation region to higher amplitudes. For an elastically mounted rigid cylinder, stable oscillations occur when $C_{y,v} = 0$ (neglecting structural damping). This means that if the model is to predict the correct free vibration amplitude, C_v should be chosen so that $C_{y,v} = 0$ at the correct y_0/D.

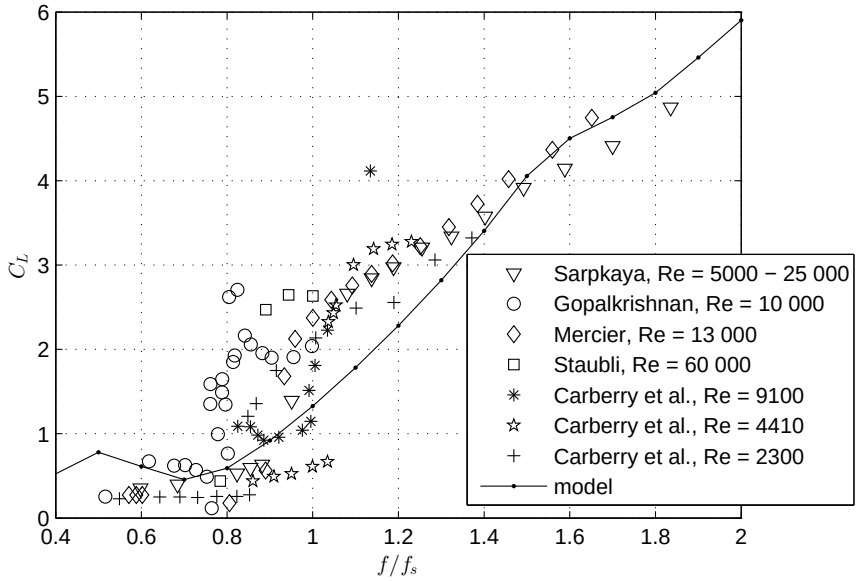

Figure 11: Total lift coefficient amplitude as a function of frequency at $y_0/D = 0.5$. The solid line is predicted by the model using $C_D = C_v = 1.2$ and $C_M = 2$, while the symbols represent the experiments by Sarpkaya [33], Gopalkrishnan [29], Mercier [34], Staubli [35] and Carberry et al. [32]. The experimental data was taken from [32].

ii) The total added mass coefficient predicted by the model is a result of the added mass term in Morison's equation and the vortex shedding force. The first term gives a constant contribution equal to $C_a = C_M - 1$, while the latter will vary depending on the phase difference between the vortex shedding force and the cylinder acceleration.

iii) The mean drag coefficient $\bar{C}_D$ depends on both C_D and C_v. When the cylinder is stationary, $\bar{C}_D = C_D$, and C_D should be chosen accordingly. When the cylinder vibrates, two effects contribute to increasing the mean drag. Firstly, the average relative velocity increases. Secondly, the vortex shedding force has a component in the direction of the flow which will have a non-zero mean value when the vortex shedding is synchronized with the cylinder motion.

iv) Although this has not been considered here, the parameters $\hat{f}_0$ and $\Delta\hat{f}$ in equation 4 can be changed, thereby altering the synchronization range of the vortex shedding force.

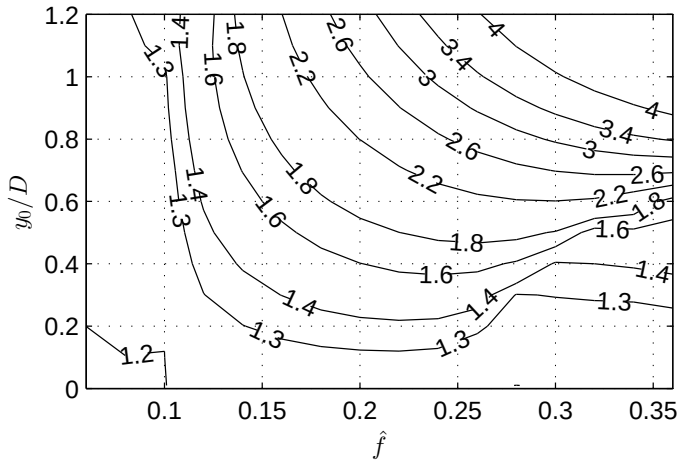

Figure 12: Mean drag coefficient predicted by the model, using $C_D = C_v = 1.2$.

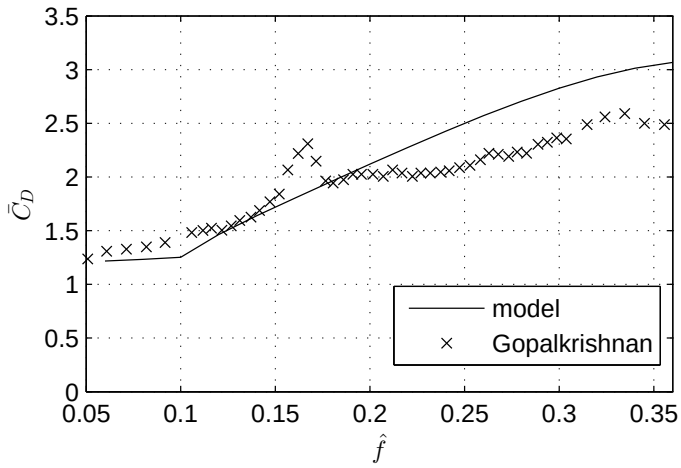

Figure 13: Mean drag coefficient for $y_0/D = 0.75$. The solid line are predicted by the model using $C_D = C_v = 1.2$, while the crosses are from experiments by Gopalkrishnan [29].

4. Structure modeling and dynamic analysis

The hydrodynamic force model has been implemented into the finite element software Simla [36], which is a tool developed for pipe-laying analyses including very large deformations, non-linear material behavior and contact. 2-node 3 dimensional beam elements are used, with 3 translational and 3 rotational degrees of freedom at each node. The beam element is based on classical theory for slender beams, assuming planes normal to the neutral axis to remain plane, as well as neglecting shear deformations due to lateral loads and lateral contraction due to axial elongation. In addition, the strains are assumed to be small. A corotational formulation is used to account for large displacements and rotations. Based on the principle of virtual work on incremental form, the element stiffness matrix contains contributions from geometric and material stiffness. The geometric contribution is the influence of axial force on the lateral stiffness of the beam. The nonlinear dynamic analysis in Simla is based on the incremental equation of motion, which is solved in time domain using the HHT-α method [37].

5. Results

5.1. Case 1: SCR in uniform current

Wang et al. [8] performed model tests to study VIV on steel catenary risers (SCRs). In these experiments, the top end of a truncated SCR model was suspended from a towing carriage, while the lower end was resting on an fake seabed made of aluminium. The riser was terminated in both ends with universal couplings, which were moment-free and torsion restricted. Strain sensors were installed at 25 equidistant points to measure the dynamic response. Important physical properties of the model riser are given in table 1. The experimental campaign consisted of two parts: Uniform current VIV and heave induced VIV. Uniform current was obtained by moving the top end and the seabed with a constant speed (on tracks).

Table 1: Properties of the riser model [8].

Riser length	23.71 m
Depth	9 m
Horizontal length	21.0425 m
Outer diameter	0.024 m
Mass per length (dry)	0.69 kg/m
Bending stiffness (EI)	10.5 Nm^2
Tensile stiffness (EA)	$6.66 \cdot 10^5$ N

The experimental campaign contained cases with current velocities ranging from 0.1 to 0.5 m/s. However, due to the restricted track length, the test duration was relatively short for the high velocity cases. With this in mind, a case with a current velocity of 0.2 m/s is chosen for the present comparison. The current direction is in the riser plane, as indicated in figure 14, which means that the VIV motion is mainly out of the riser plane (i.e. the cross-flow direction). As previously stated, this study focuses on the prediction of cross-flow VIV, and for this reason only the cross-flow strains are analyzed. Figure 15 shows the dynamic part of the measured cross-flow strain from the experiment by Wang et al. [8]. Note that the strain sensors were mounted at a diameter $D = 19.5$ mm, and the measured values have been adjusted to show the strain at the outer surface ($D = 24$ mm). The initial transient has been removed, and the data in figure 15 is from the time window with fully developed VIV. Waves are seen traveling towards the bottom end (which is located at $x = 0$), and the vibration pattern is relatively stationary, although some irregularities are seen. It is also quite clear that a single frequency dominates.

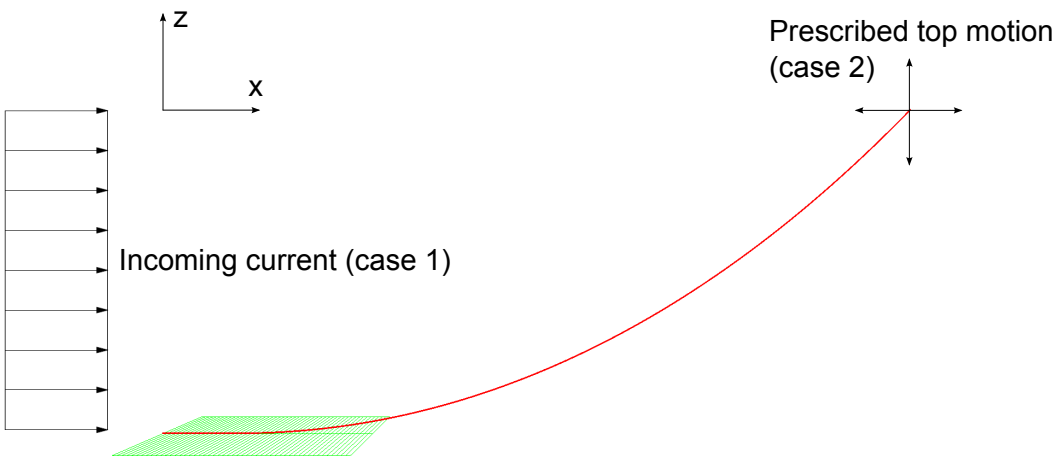

Figure 14: Finite element model in the static configuration.

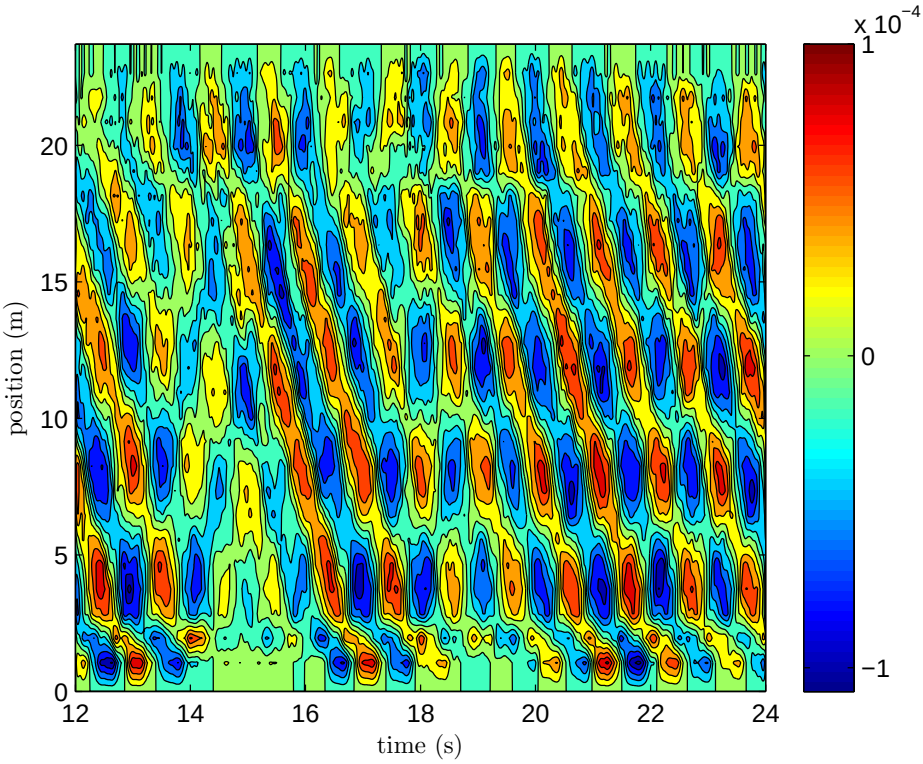

Figure 15: From experiment by Wang et al. [8] (constant uniform flow): Dynamic cross-flow strain along the riser as a function of time.

A finite element model of the SCR is established using the previously described software, Simla. The SCR is discretized into 500 beam elements (a convergence test was performed by doubling the number of elements). An initial static analysis is performed, including weight, buoyancy and a prescribed top-end displacement in the x-direction to obtain the desired static configuration. The FE model after the completion of the static analysis is seen in figure 14. Seabed contact is modeled using nonlinear springs with a vertical stiffness of 1 (kN/m)/m in compression. This is very stiff compared to the SCR, and represents a nearly rigid surface. The seabed spring stiffness in tension is zero, which means the SCR is allowed to lift freely from the seabed. When a node of the SCR is in contact with the seabed, it will also experience friction forces in the axial and lateral directions, which will restrain the riser from sliding until the friction force exceeds the vertical contact force multiplied by a friction coefficient. In the analysis, the seabed-riser friction coefficient is set to 0.2. The exact number is not known, but 0.2 is a reasonable value for plastic and aluminium in water. For the dynamic analysis, a time step of 0.005 s is applied, which was found to be sufficient (i.e. reducing the time step gave no change in the results).

The hydrodynamic forces are calculated according to the described model (equation (13)). The Reynolds number for the case considered here is approximately 3 000, based on the maximum normal flow velocity. Swithenbank et al. [38] have shown that the VIV response amplitude for flexible cylinders depends on the Reynolds number, and this must be kept in mind when choosing a value for C_v. As stated in section 3, a suitable strategy would be to choose C_v such that the maximum amplitude of the positive excitation zone (i.e. the region where $C_{y,v}$ is positive) is correct, compared to experiments. For Re = 10 000, the maximum y_0/D which gives positive excitation is approximately 0.85, according to Gopalkrishnan [29]. Based on [38], the maximum amplitude at $Re = 3\ 000$ is reduced to 60% compared to $Re = 10\ 000$. Assuming that the maximum response amplitude for a flexible cylinder is linearly related to the maximum y_0/D of the

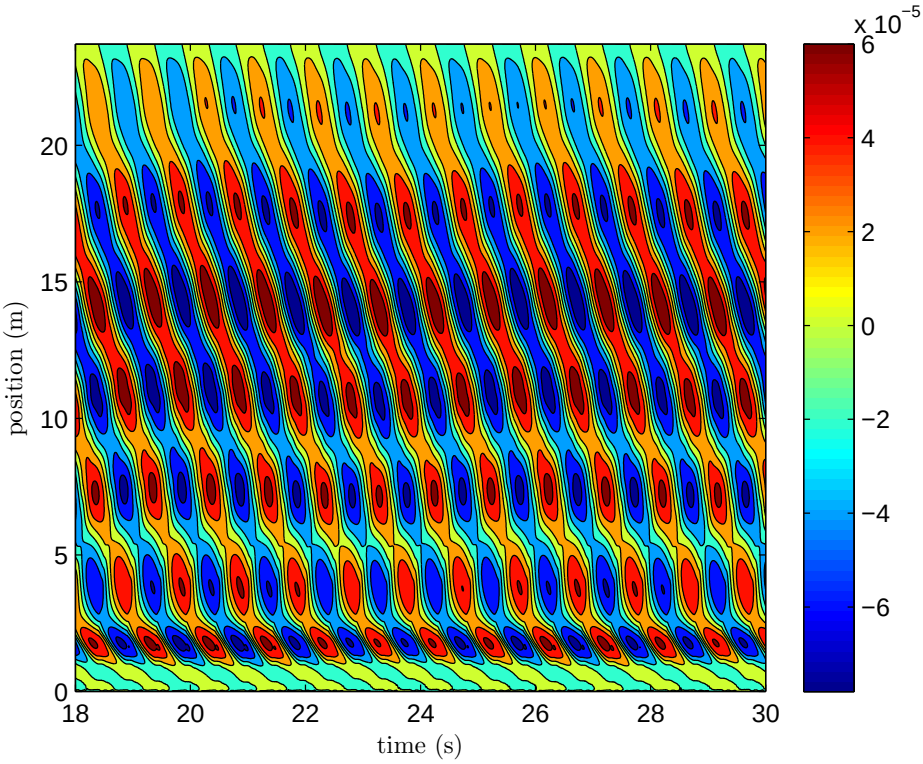

Figure 16: From simulation (constant uniform flow): Dynamic cross-flow strain along the riser as a function of time.

positive excitation zone, it follows that the positive excitation zone extends up to $y_0/D = 0.85 \cdot 0.6 \approx 0.5$ for Re = 3 000. This corresponds to $C_v = 0.7$ (found by plotting figure 6 using different values for C_v), which is used in the subsequent simulations. The drag and inertia coefficients are set to $C_D = 1.2$ and $C_M = 2$, meaning that the drag coefficient is assumed to be independent of the angle of attack. Experiments have shown [39] that this is a good approximation for angles larger than 5 degrees. This means that, for the present SCR in uniform flow, the independence principle is violated close to the bottom. This is however only a small part of the riser, and is therefore not expected to cause significant errors.

The dynamic cross-flow strain from the simulation is shown in figure 16. Compared to the experimental results, the same type of traveling waves are seen. 7 distinctive peaks are seen along the riser span, while in the experimental results, there are only 6 peaks. This indicates that the predicted mode of vibration is one number higher than in the experiment, which may be caused by a mismatch in the added mass. This is however a small error, and some uncertainty in the predicted mode must be expected. Furthermore, the predicted vibration pattern is more regular than in the experiment, which is also unsurprising, due to the simplifications embedded in the model. The magnitude of the predicted strains are compared to the experimental results in figure 17, in terms of the r.m.s. of the dynamic cross-flow strain along the riser. The agreement along the riser span is reasonable, although some discrepancies are seen. The maximum r.m.s. of strain predicted by the model is 99.6 % of the experimentally observed value. However, the point of maximum strain in the simulation is not the same as in the experiment. The power spectrum of the strain signals from the experiment and simulation are shown and compared in figure 18. It is seen that the dominating frequencies are almost exactly the same, although the predicted spectrum is slightly more narrow-banded. The secondary frequency peak in the experimental data may be a result of variations in amplitude and frequency, as the response at any given point along the SCR is not perfectly sinusoidal (see figure 15).

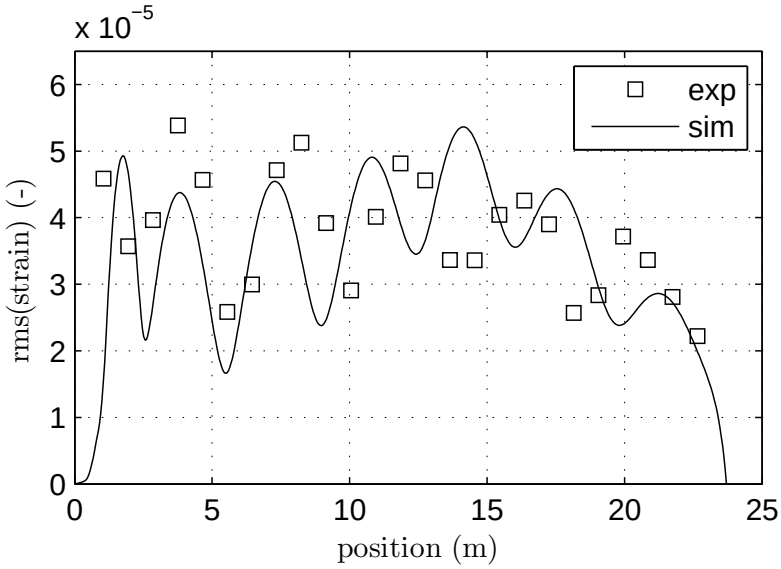

Figure 17: Comparison between predicted (solid line) and measured (squares) r.m.s. of dynamic cross-flow strain along the riser (constant uniform flow).

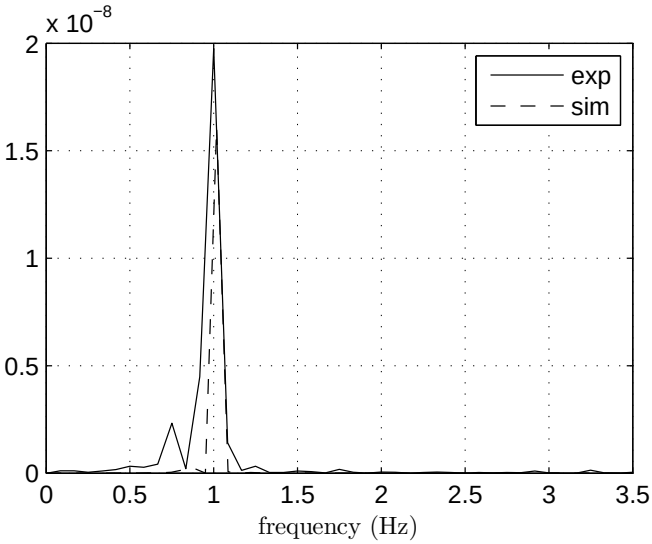

Figure 18: Frequency spectrum of dynamic cross-flow strain from simulation and experiment (constant uniform flow) 8.25 meters from the lower end.

5.2. Case 2: Heave induced VIV of SCR

Wang et al. [8] used the same experimental set up to study heave induced VIV, caused by a forced oscillating movement of the upper end of the riser, as indicated in figure 14. The SCR model was oscillating in still water, and the relative velocity between the riser and the surrounding water caused vortex shedding and VIV. The cross-flow strains measured in the test are shown in figure 19 together with the x (horizontal) and z (vertical) displacement of the top point. Note that the strain signal has been band-pass filtered to remove high-frequency noise and the low-frequency component associated with the heave motion. The top-end motion is approximately sinusoidal with a period of 5.96 s. Compared to the constant current case, the VIV response appears more irregular, which is expected due to the relative oscillating flow. Although the spatial resolution is limited, it is possible to see how the touch-down point of the SCR (located close to $x = 0$) is moving as the lower end of the riser lifts up and falls down towards the bottom repeatedly.

The r.m.s. of the in-plane velocity (i.e. the relative flow velocity causing VIV) along the riser according to the simulation model is shown in figure 20. When the flow velocity varies both in time and space, there is no unique Reynolds number, which can make it difficult to choose a single value for C_v. However, the maximum of the r.m.s. of the in-plane velocity may be a reasonable choice for a characteristic velocity. From figure 20, this is found to be 0.16 m/s, which means the Reynolds number is approximately 4 000. This is slightly larger than in the preceding case, and based on [38], the maximum response is expected to be around 70 % of the value at Re = 10 000. Following the same way of thinking as for the previous case, this means that $C_v = 0.8$ approximately, and this value is adopted in the simulations. As in the previous case, $C_D = 1.2$ and $C_M = 2$. Apart from the boundary conditions at the top, the structural model is also the same as before.

The cross-flow bending strains found from the simulation are shown in figure 21, together with the x (horizontal) and z (vertical) displacement of the top end node. The prescribed motion of the top node is exactly the same as measured in the experiment. The predicted vibration pattern looks qualitatively similar to the experimental results, and consists of irregular traveling waves. It is seen that the peak close to the touch-down point moves back and forth due to the variation in bottom contact. The predicted r.m.s. of the cross-flow strains are compared to the experiment in figure 22, and the comparison shows that the magnitude of the strain is somewhat over-predicted for the lower part and under-predicted for the upper half. Compared to the experiment, the maximum r.m.s. of strain predicted by the model is 6 % too high. To get a better understanding of the frequency content in the response, the measured and predicted cross-flow strain at a point 8.25 meters from the lower end are shown in figure 23 and 24 together with a wavelet plot of the strain signals. The wavelet plot shows the frequency content as a function of time, and from figure 23 it is seen that the dominating frequency in the experiment is close to 1 Hz. Less pronounced frequencies are seen at all times, both below and above the dominating ones. It is also noted that the amplitude in the experiment is relatively small at $t = 30$ s, but increases around $t = 36$ s for some unknown reason. The amplitude of the predicted strain shown in figure 24 is more stable. The predicted dominating frequency is also close to 1 Hz, and other frequency components are present at lower and higher frequencies, as in the experiment.

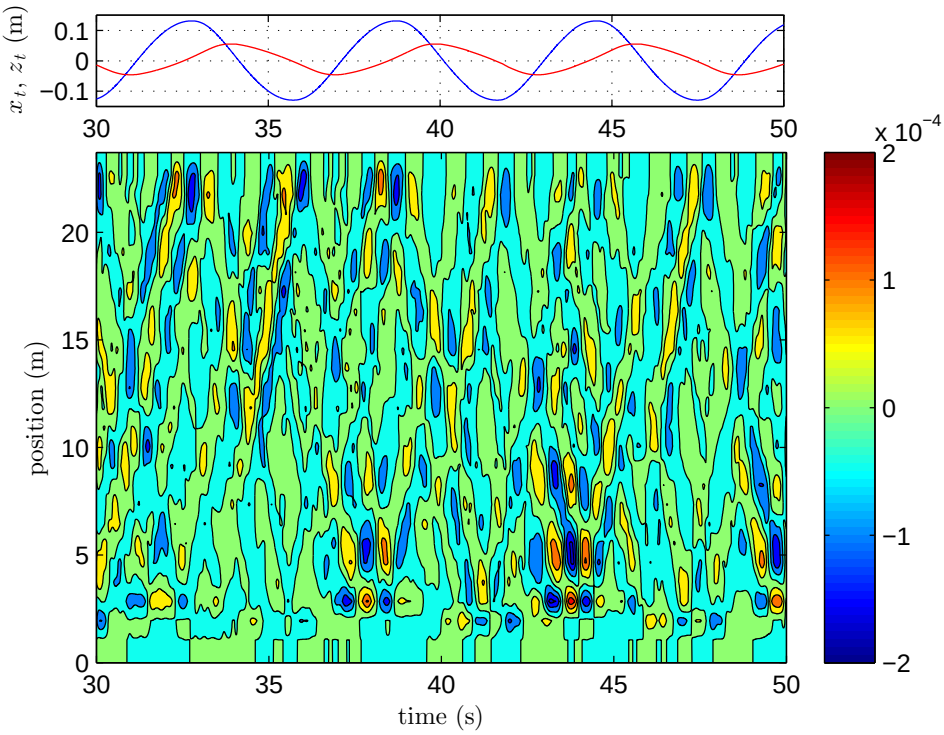

Figure 19: From experiment by Wang et al. [8] (heave induced VIV): Dynamic cross-flow strain along the riser as a function of time. The top figure shows the x (red) and z (blue) displacement of the riser's upper end. Note that the strain signal has been band-pass filtered to remove high-frequency noise and the low-frequency component associated with the heave motion.

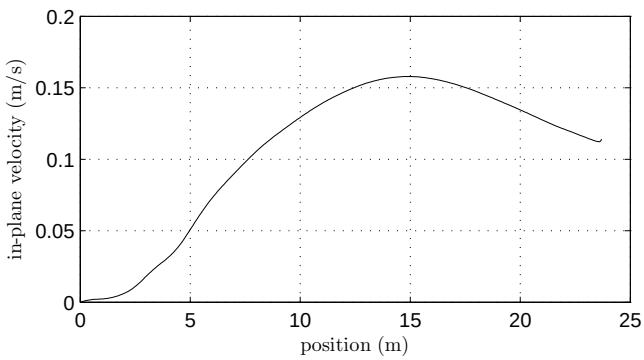

Figure 20: R.m.s. of riser in-plane velocity (calculated).

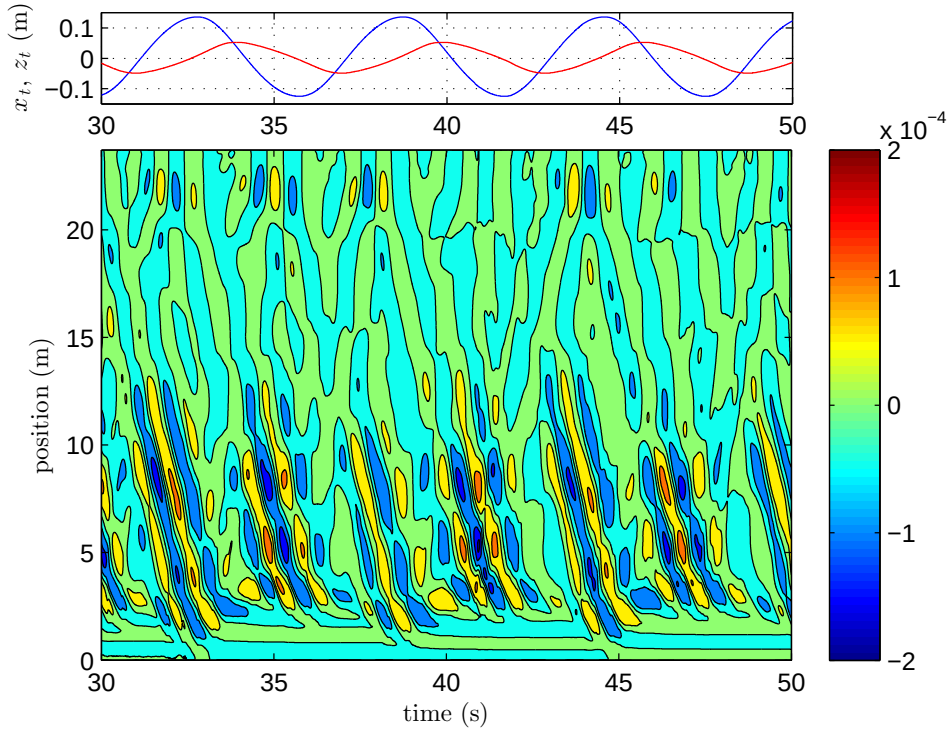

Figure 21: From simulation (heave induced VIV): Dynamic cross-flow strain along the riser as a function of time. The top figure shows the x (red) and z (blue) displacement of the riser's upper end.

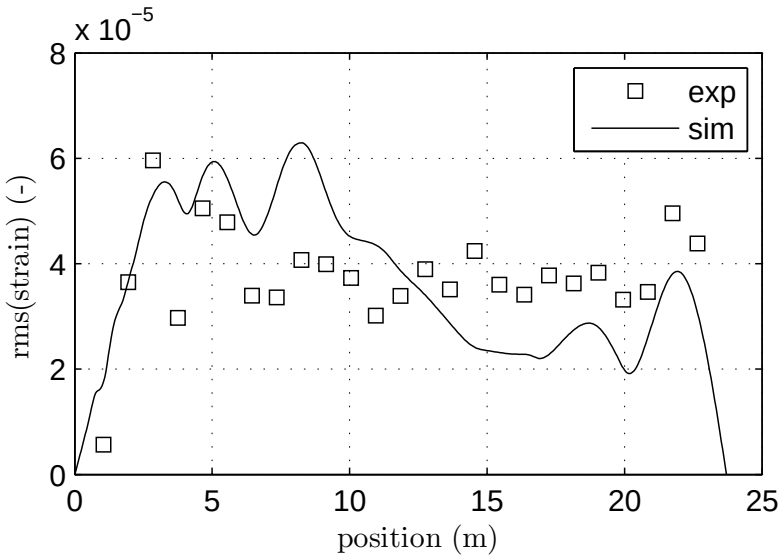

Figure 22: Comparison between predicted (solid line) and measured (squares) r.m.s. of dynamic cross-flow strain along the riser (heave induced VIV).

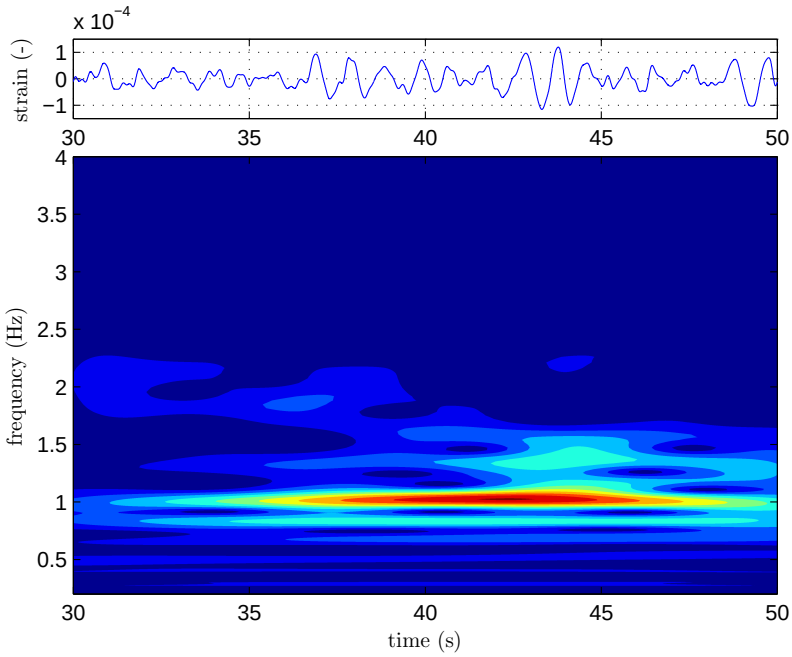

Figure 23: From experiment by Wang et al. [8] (heave induced VIV): The top figure shows the dynamic cross-flow strain 8.25 meters from the lower end. The bottom figure shows the wavelet contour plot of the strain signal.

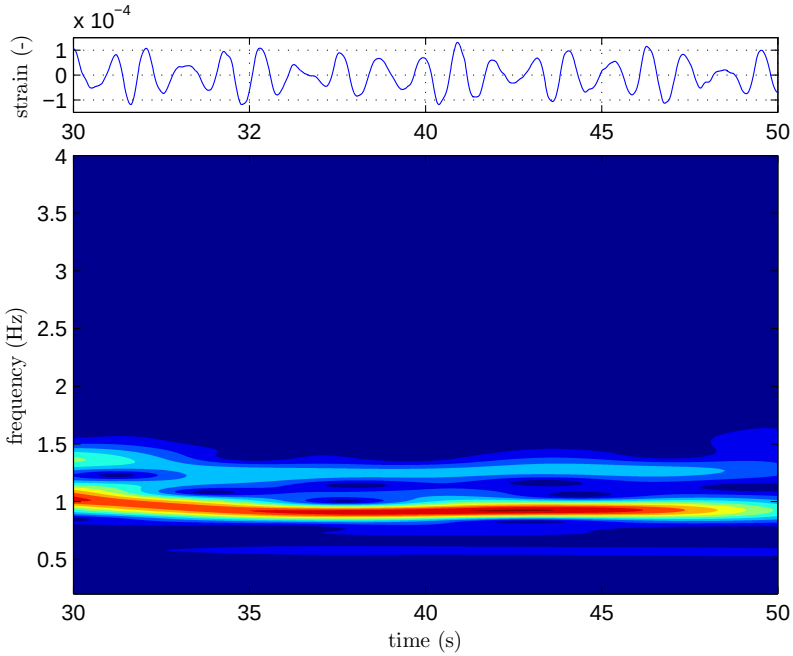

Figure 24: From simulation (heave induced VIV): The top figure shows the dynamic cross-flow strain 8.25 meters from the lower end. The bottom figure shows the wavelet contour plot of the strain signal.

6. Conclusions

A method for time domain analysis of cross-flow VIV of slender structures exposed to currents and prescribed motions has been presented, which is able to account for non-linear structural effects such as large displacements and time varying contact conditions. The hydrodynamic loading is computed based on Morison's equation and a semi-empirical formulation of the cross-flow vortex shedding force [18]. It is shown that the model provides a realistic description of the cross-flow energy transfer and added mass as well as the experimentally observed drag amplification, using constant hydrodynamic coefficients. Next, the combined hydrodynamic and structural model is applied to simulate VIV of the model scale SCR tested by Wang et al. [8]. Two different conditions are considered, namely uniform stationary current and heave induced VIV. In the first case, the response is almost stationary with a single dominating frequency. Both the magnitude and the frequency content of the dynamic cross-flow strain is accurately predicted by the model. In the second case, the relative fluid velocity is oscillating, due to the sinusoidal motion prescribed at the top end of the riser. This causes an irregular response pattern with multiple frequencies and varying amplitudes. Similar behavior is seen in the simulation and the experiment, and the dominating frequency and the r.m.s. of strain is quite accurately captured. This indicates that the present hydrodynamic load model provides a good approximation of the relevant loads, which makes it possible to simulate riser VIV with a high degree of realism, when combined with a non-linear finite element program.

Acknowledgments

The authors gratefully acknowledge Statoil for permission to use the data from the experiments performed at Shanghai Jiao Tong University. We would also like to thank Elizabeth Passano, Jie Wu, Decao Jin, Shixiao Fu and Halvor Lie at MARINTEK for contributing with valuable discussions regarding VIV in general, as well as sharing their knowledge about the SCR experiment.

References

[1] R. D. Blevins, Flow-Induced Vibration, 2nd Edition, Van Nostrand Reinhold, 1990.
[2] C. Feng, The measurement of vortex induced effects in flow past stationary and oscillating circular and D-section cylinders, Master's thesis, University of British Columbia (1968).
[3] J. K. Vandiver, V. Jaiswal, V. Jhingran, Insights on vortex-induced, traveling waves on long risers, Journal of Fluids and Structures 25 (4) (2009) 641–653.
[4] R. Bourguet, G. E. Karniadakis, M. S. Triantafyllou, Vortex-induced vibrations of a long flexible cylinder in shear flow, Journal of Fluid Mechanics 677 (2011) 342–382.
[5] C. M. Larsen, H. Lie, E. Passano, R. Yttervik, J. Wu, G. Baarholm, VIVANA - Theory Manual, Version 3.7 (2009).
[6] M. Triantafyllou, G. Triantafyllou, Y. Tein, B. D. Ambrose, et al., Pragmatic riser VIV analysis, in: Offshore Technology Conference, Offshore Technology Conference, 1999.
[7] J. K. Vandiver, L. Li, SHEAR7 V4.4 Program Theoretical Manual (2005).
[8] J. Wang, S. Fu, R. Baarholm, J. Wu, C. M. Larsen, Fatigue damage of a steel catenary riser from vortex-induced vibration caused by vessel motions, Marine Structures 39 (2014) 131–156.
[9] A. Ortega, A. Rivera, O. J. Nydal, C. M. Larsen, On the dynamic response of flexible risers caused by internal slug flow, in: ASME 2012 31st International Conference on Ocean, Offshore and Arctic Engineering, American Society of Mechanical Engineers, 2012, pp. 647–656.
[10] R. Bishop, A. Hassan, The lift and drag forces on a circular cylinder oscillating in a flowing fluid, Proceedings of the Royal Society of London. Series A. Mathematical and Physical Sciences 277 (1368) (1964) 51–75.
[11] R. Gabbai, H. Benaroya, An overview of modeling and experiments of vortex-induced vibration of circular cylinders, Journal of Sound and Vibration 282 (3) (2005) 575–616.
[12] N. Srinil, Multi-mode interactions in vortex-induced vibrations of flexible curved/straight structures with geometric non-linearities, Journal of Fluids and Structures 26 (7) (2010) 1098–1122.
[13] R. Ogink, A. Metrikine, A wake oscillator with frequency dependent coupling for the modeling of vortex-induced vibration, Journal of Sound and Vibration 329 (26) (2010) 5452–5473.
[14] H. Lie, A time domain model for simulation of vortex induced vibrations on a cable, in: Proc. Sixth Int. Conf. on Flow Induced Vibrations, London, UK, 1995, pp. 455–466.
[15] L. Finn, K. Lambrakos, J. Maher, Time domain prediction of riser VIV, in: Proceedings of the Fourth International Conference on Advances in Riser Technologies, 1999.
[16] P. Mainçon, A Wiener-Laguerre Model of VIV Forces Given Recent Cylinder Velocities, Mathematical Problems in Engineering 2011 (414702) (2011) 43 pages.

[17] H. Xue, K. Wang, W. Tang, A practical approach to predicting cross-flow and in-line VIV response for deepwater risers, Applied Ocean Research 52 (2015) 92 – 101.
[18] M. J. Thorsen, S. Sævik, C. M. Larsen, A simplified method for time domain simulation of cross-flow vortex-induced vibrations, Journal of Fluids and Structures 49 (2014) 135–148.
[19] M. J. Thorsen, S. Sævik, C. M. Larsen, Time domain simulation of cross-flow and in-line vortex-induced vibrations, in: Proceedings of EURODYN 2014, Porto, Portugal, 2014.
[20] M. J. Thorsen, S. Sævik, C. M. Larsen, Fatigue damage from time domain simulation of combined in-line and cross-flow vortex-induced vibrations, Marine Structures 41 (2015) 200–222.
[21] M. J. Thorsen, S. Sævik, C. M. Larsen, Time domain simulation of vortex-induced vibrations based on phase-coupled oscillator synchronization, in: ASME 2015 34th International Conference on Ocean, Offshore and Arctic Engineering, American Society of Mechanical Engineers, 2015.
[22] M. J. Thorsen, S. Sævik, C. M. Larsen, Time domain simulation of vortex-induced vibrations in stationary and oscillating flows, Journal of Fluids and Structures 61 (2016) 1 – 19.
[23] O. Faltinsen, Sea loads on ships and offshore structures, Vol. 1, Cambridge university press, 1993.
[24] B. M. Sumer, J. Fredsøe, Hydrodynamics around cylindrical structures, Vol. 12, World Scientific Publishing Company, 1997.
[25] C. Norberg, Fluctuating lift on a circular cylinder: review and new measurements, Journal of Fluids and Structures 17 (1) (2003) 57–96.
[26] C. Williamson, A. Roshko, Vortex formation in the wake of an oscillating cylinder, Journal of Fluids and Structures 2 (4) (1988) 355–381.
[27] N. Jauvtis, C. Williamson, The effect of two degrees of freedom on vortex-induced vibration at low mass and damping, Journal of Fluid Mechanics 509 (6) (2004) 23–62.
[28] S. H. Strogatz, From Kuramoto to Crawford: exploring the onset of synchronization in populations of coupled oscillators, Physica D: Nonlinear Phenomena 143 (1–4) (2000) 1 – 20.
[29] R. Gopalkrishnan, Vortex-induced forces on oscillating bluff cylinders, Ph.D. thesis, Massachusetts Institute of Technology (1993).
[30] H. Mukundan, Vortex-induced vibration of marine risers: motion and force reconstruction from field and experimental data, Ph.D. thesis, Massachusetts Institute of Technology (2008).
[31] K. Vikestad, Multi-frequency response of a cylinder subjected to vortex shedding and support motions, Ph.D. thesis, Norwegian University of Science and Technology, Department of Marine Technology (1998).
[32] J. Carberry, J. Sheridan, D. Rockwell, Controlled oscillations of a cylinder: forces and wake modes, Journal of Fluid Mechanics 538 (2005) 31–69.
[33] T. Sarpkaya, Hydrodynamic damping, flow-induced oscillations, and biharmonic response, Journal of offshore Mechanics and Arctic engineering 117 (4) (1995) 232–238.
[34] J. A. Mercier, Large amplitude oscillations of a circular cylinder in a low-speed stream, Stevens Institute of Technology, PhD.
[35] T. Staubli, Calculation of the vibration of an elastically mounted cylinder using experimental data from forced oscillation, Journal of Fluids Engineering 105 (2) (1983) 225–229.
[36] S. Sævik, SIMLA Theory Manual (2008).
[37] H. M. Hilber, T. J. Hughes, R. L. Taylor, Improved numerical dissipation for time integration algorithms in structural dynamics, Earthquake Engineering & Structural Dynamics 5 (3) (1977) 283–292.
[38] S. B. Swithenbank, J. K. Vandiver, C. M. Larsen, H. Lie, Reynolds number dependence of flexible cylinder VIV response data, in: ASME 2008 27th International Conference on Offshore Mechanics and Arctic Engineering, American Society of Mechanical Engineers, 2008, pp. 503–511.
[39] S. Ersdal, O. Faltinsen, Normal forces on cylinders in near-axial flow, Journal of Fluids and Structures 22 (8) (2006) 1057 – 1077.